LETTER

Observation of a discrete time crystal

J. Zhang[1], P. W. Hess[1], A. Kyprianidis[1], P. Becker[1], A. Lee[1], J. Smith[1], G. Pagano[1], I.-D. Potirniche[2], A. C. Potter[3], A. Vishwanath[2,4], N. Y. Yao[2] & C. Monroe[1,5]

Spontaneous symmetry breaking is a fundamental concept in many areas of physics, including cosmology, particle physics and condensed matter[1]. An example is the breaking of spatial translational symmetry, which underlies the formation of crystals and the phase transition from liquid to solid. Using the analogy of crystals in space, the breaking of translational symmetry in time and the emergence of a 'time crystal' was recently proposed[2,3], but was later shown to be forbidden in thermal equilibrium[4–6]. However, non-equilibrium Floquet systems, which are subject to a periodic drive, can exhibit persistent time correlations at an emergent subharmonic frequency[7–10]. This new phase of matter has been dubbed a 'discrete time crystal'[10]. Here we present the experimental observation of a discrete time crystal, in an interacting spin chain of trapped atomic ions. We apply a periodic Hamiltonian to the system under many-body localization conditions, and observe a subharmonic temporal response that is robust to external perturbations. The observation of such a time crystal opens the door to the study of systems with long-range spatio-temporal correlations and novel phases of matter that emerge under intrinsically non-equilibrium conditions[7].

For any symmetry in a Hamiltonian system, its spontaneous breaking in the ground state leads to a phase transition[11]. The broken symmetry itself can assume many different forms. For example, the breaking of spin-rotational symmetry leads to a phase transition from paramagnetism to ferromagnetism when the temperature is brought below the Curie point. The breaking of spatial symmetry leads to the formation of crystals, where the continuous translational symmetry of space is replaced by a discrete one.

We now pose an analogous question: can the translational symmetry of time be broken? The proposal of such a 'time crystal'[2] for time-independent Hamiltonians has led to much discussion[12], with the conclusion that such structures cannot exist in the ground state or any thermal equilibrium state of a quantum mechanical system[4–6]. A simple intuitive explanation is that quantum equilibrium states have time-independent observables by construction; thus, time translational symmetry can only be spontaneously broken in non-equilibrium systems[7–10]. In particular, the dynamics of periodically driven Floquet systems possesses a discrete time translational symmetry governed by the drive period. This symmetry can be further broken into 'super-lattice' structures where physical observables exhibit a period larger than that of the drive[13]. Such a response is analogous to commensurate charge density waves that break the discrete translational symmetry of their underlying lattice[1]. The robust subharmonic synchronization of the many-body Floquet system is the essence of the discrete time crystal (DTC) phase[7–10]. In a DTC, the underlying Floquet drive should generally be accompanied by strong disorder, leading to many-body localization[14] and thereby preventing the quantum system from absorbing the drive energy and heating to infinite temperatures[15–17]. We note that under certain conditions, time crystal dynamics can persist for rather long times even in the absence of localization before ultimately being destroyed by thermalization[18].

Here we report the direct observation of discrete time translational symmetry breaking and DTC formation in a spin chain of trapped atomic ions, under the influence of a periodic Floquet many-body localization (MBL) Hamiltonian. We experimentally implement a quantum many-body Hamiltonian with long-range Ising interactions and disordered local effective fields, using optical control techniques[19,20]. Following the evolution through many Floquet periods, we measure the temporal correlations of the spin magnetization dynamics.

A DTC requires the ability to control the interplay between three key ingredients: strong drive, interactions and disorder. These are reflected in the applied Floquet Hamiltonian H, consisting of the following three successive pieces with overall period $T = t_1 + t_2 + t_3$ (see Fig. 1) ($\hbar = 1$):

$$H = \begin{cases} H_1 = g(1-\varepsilon) \sum_i \sigma_i^y & \text{time } t_1 \\ H_2 = \sum_i J_{ij} \sigma_i^x \sigma_j^x & \text{time } t_2 \\ H_3 = \sum_i D_i \sigma_i^x & \text{time } t_3 \end{cases} \qquad (1)$$

Here, σ_i^γ ($\gamma = x, y, z$) is the Pauli matrix acting on the ith spin, g is the Rabi frequency with small perturbation ε, $2gt_1 = \pi$, J_{ij} is the coupling strength between spins i and j, and D_i is a site-dependent disordered potential sampled from a uniform random distribution with $D_i \in [0, W]$.

To implement the Floquet Hamiltonian, each of the effective spin-1/2 particles in the chain is encoded in the $^2S_{1/2} |F=0, m_F=0\rangle$ and $|F=1, m_F=0\rangle$ hyperfine 'clock' states of a $^{171}Yb^+$ ion, denoted $|\downarrow\rangle_z$ and $|\uparrow\rangle_z$ and separated by 12.642831 GHz (F and m_F denote the hyperfine and Zeeman quantum numbers, respectively). We store a chain of
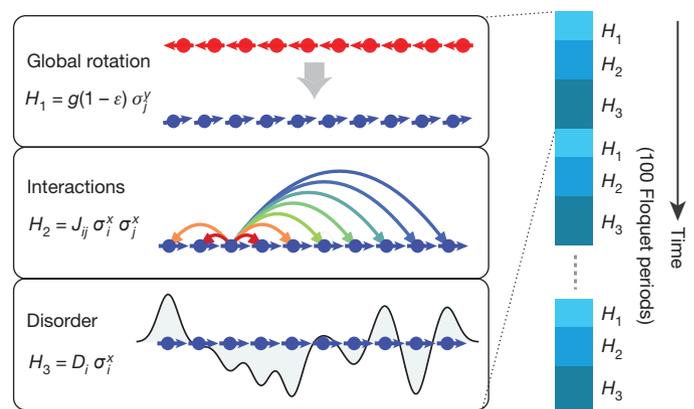
Figure 1 | Floquet evolution of a spin chain. Three Hamiltonians are applied sequentially in time: a global spin rotation of nearly π (H_1), long-range Ising interactions (H_2), and strong disorder (H_3) (left). The system evolves for 100 Floquet periods of this sequence (right). On the left, circles with arrows denote spins (that is, ions 1 to 10), where the red colour denotes initial magnetization. Curved coloured lines between spins denote the spin–spin interactions, and the black trace illustrates the applied disorder.

[1]Joint Quantum Institute, University of Maryland Department of Physics and National Institute of Standards and Technology, College Park, Maryland 20742, USA. [2]Department of Physics, University of California Berkeley, Berkeley, California 94720, USA. [3]Department of Physics, University of Texas at Austin, Austin, Texas 78712, USA. [4]Department of Physics, Harvard University, Cambridge, Massachusetts 02138, USA. [5]IonQ, Inc., College Park, Maryland 20742, USA.

10 ions in a linear radio frequency Paul trap, and apply single spin rotations using optically driven Raman transitions between the two spin states. Spin–spin interactions are generated by spin-dependent optical dipole forces, which give rise to a tunable long-range Ising coupling[21] that falls off approximately algebraically as $J_{ij} \propto J_0/|i-j|^\alpha$. Programmable disorder among the spins is generated by the ac Stark shift from a tightly focused laser beam that addresses each spin individually[20]. The Stark shift is an effective site-dependent σ_i^z field, so in order to transform it into the x direction of the Bloch sphere we surround this operation with $\pi/2$ pulses (see Methods). Finally, we measure the magnetization of each spin by collecting the spin-dependent fluorescence on a camera for site-resolved imaging. This allows access to the single-site magnetization, σ_i^γ, along any direction with a detection fidelity >98% per spin. The unitary time evolution under a single Floquet period is:

$$U(T) = e^{-iH_3 t_3} e^{-iH_2 t_2} e^{-iH_1 t_1} \qquad (2)$$

The first evolution operator $e^{-iH_1 t_1}$ nominally flips all the spins around the y-axis of the Bloch sphere by an angle $2gt_1 = \pi$, but also includes a controlled perturbation in the angle, $\varepsilon\pi$, where $\varepsilon < 0.15$. This critical rotation step is susceptible to noise in the Rabi frequency (1% r.m.s.) from laser intensity instability, and also optical inhomogeneities (<5%) across the chain due to the shape of the Raman laser beams. In order to accurately control H_1, we use the BB1 dynamical decoupling echo sequence[22] (see Methods) to suppress these effects, resulting in control

of the rotation angle to a precision <0.5%. The second evolution operator $e^{-iH_2 t_2}$ applies the spin–spin Ising interaction, where the maximum nearest-neighbour coupling J_0 ranges from $2\pi(0.04\,\text{kHz})$ to $2\pi(0.25\,\text{kHz})$ and decays with distance at a power law exponent $\alpha = 1.5$. The duration of the interaction term is set so that $J_0 t_2 < 0.04$ rad of phase accumulation. The third evolution operator $e^{-iH_3 t_3}$ provides disorder to localize the system, and is programmed so that the variance of the disorder is set by $Wt_3 = \pi$. In this regime, MBL is expected to persist even in the presence of long-range interactions[23,24].

To observe the DTC, we initialize the spins to the state $|\psi_0\rangle = |\downarrow\rangle_x = \frac{1}{\sqrt{2}}\big(|\downarrow\rangle_z + |\uparrow\rangle_z\big)$ through optical pumping followed by a global $\pi/2$ rotation. After many periods of the above Floquet unitary equation (2), we measure the magnetization of each spin along x, which gives the time-correlation function:

$$\langle \sigma_i^x(t) \rangle = \langle \psi_0 | \sigma_i^x(t)\sigma_i^x(0) | \psi_0 \rangle$$

Figure 2 depicts the measured spin magnetization dynamics, both in the time and the frequency domain, up to $N = 100$ Floquet periods. A single Floquet period T is set to a value between $74\,\mu s$ and $75\,\mu s$, depending on the parameters in the Hamiltonian.

The global π-pulse $e^{-iH_1 t_1}$ rotates the spins roughly half way around the Bloch sphere, so that we expect a response of the system at twice the drive period $2T$, or half the Floquet frequency. The frequency of this subharmonic response in the magnetization is sensitive to the precise value of the global rotation in H_1 and is therefore expected to
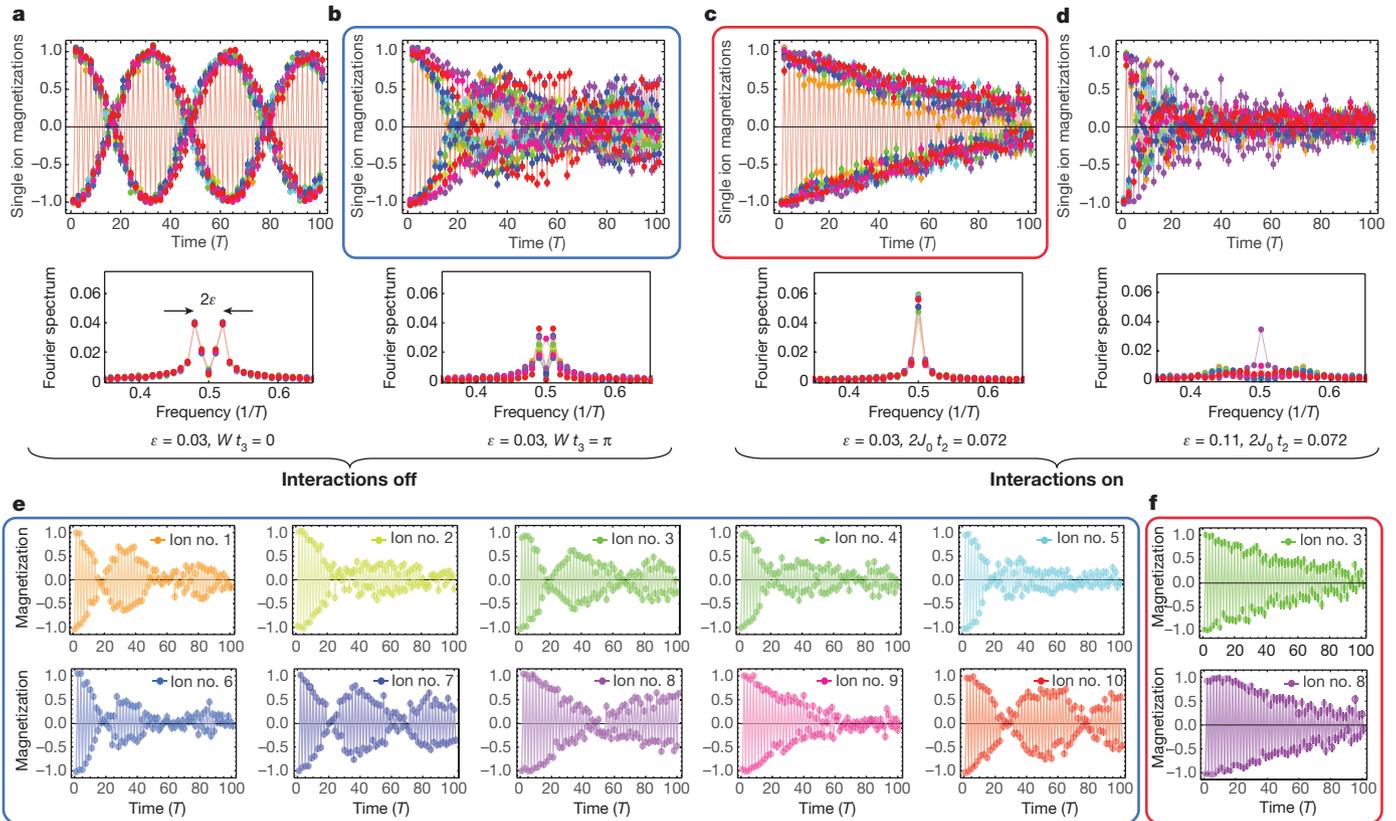
Figure 2 | Spontaneous breaking of discrete time translational symmetry. Time-evolved magnetizations of each spin $\langle \sigma_i^x(t) \rangle$ and their Fourier spectra are displayed, showing the subharmonic response of the system to the Floquet Hamiltonian. **a**, When only the H_1 spin flip is applied, the spins oscillate with a subharmonic response that beats owing to the perturbation $\varepsilon = 0.03$ from perfect π pulses, with a clear splitting in the Fourier spectrum. Wt_3 denotes the maximum phase accumulated by the disorder, which is fixed to π throughout the experiment. **b**, With both the H_1 spin flip and the disorder H_3, the spins precess with various Larmor rates in the presence of different individual fields. **c**, Finally, adding the

spin–spin interaction term H_2 (shown with the largest interaction $2J_0 t_2 = 0.072$), the spins lock to the subharmonic frequency of the drive period. Here the Fourier spectrum merges into a single peak even in the face of perturbation ε on the spin flip H_1. **d**, When the perturbation is too strong ($\varepsilon = 0.11$), we cross the boundary from the DTC into a symmetry unbroken phase[10]. **e**, Spin magnetization for all 10 spins corresponding to the case of **b**, indicated by blue box. **f**, Spins of ions 3 and 8 corresponding to the case of **c**, indicated by red box. Each point is the average of 150 experimental repetitions. Error bars are computed from quantum projection noise and detection infidelities.
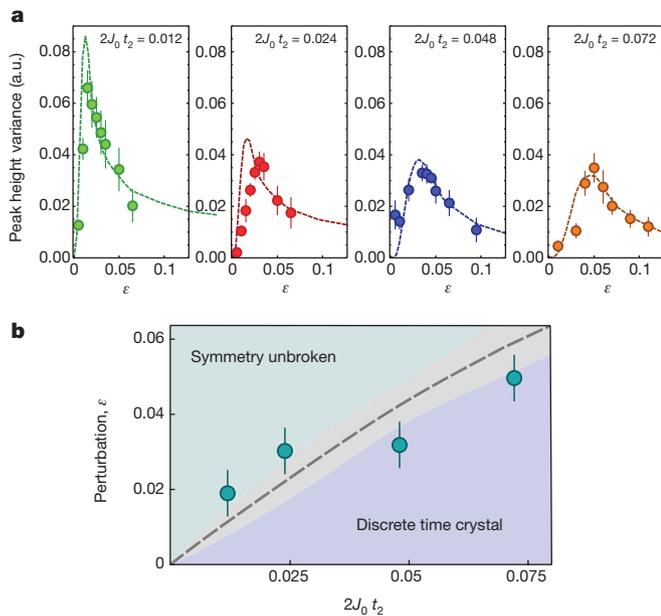
Figure 3 | Variance of the subharmonic peak amplitude as a signature of the DTC transition. a, Variances of the central peak height, computed over the 10 sites and averaged over 10 instances of disorder, for four different strengths of the long-range interaction term J_0. The crossover from a symmetry unbroken state to a DTC is observed as a peak in the measured variance of the subharmonic system response. Dashed lines, numerical results, scaled vertically to fit the experimental data (see Methods for detailed analysis procedures and possible sources of decoherence). Experimental error bars, s.e.m.; a.u., arbitrary units. **b**, Crossover determined by a fit to the variance peak location (filled circles). Dashed line, numerically determined phase boundary with experimental long-range coupling parameters[10]. Grey shaded region indicates 90% confidence level of the DTC to symmetry unbroken phase boundary. Interaction strengths are normalized to be unitless, referencing to the fixed disorder accumulated phase π (ref. 10).

track the perturbation ε. This results in coherent beats and a splitting in the Fourier spectrum by 2ε (Fig. 2a). When we add disorder $e^{-iH_3 t_3}$ to the Floquet period, the single spins precess at different Larmor rates (Fig. 2e) and dephase with respect to each other (Fig. 2b). Only on adding Ising interactions $e^{-iH_2 t_2}$, and hence many-body correlations, the spin synchronization is restored (Fig. 2c, f).

The key result is that with all of these elements, the temporal response is locked to twice the Floquet period, even in the face of perturbations to the drive in H_1. This can be seen clearly as the split Fourier peaks from Fig. 2b merge into a single peak in Fig. 2c. This represents the 'rigidity' of the DTC[10], which persists under moderate perturbation strengths. However, for large ε, the DTC phase disappears, as evinced by the decay of the subharmonic temporal correlations and the suppression of the central peak heights, as shown in Fig. 2d. In the thermodynamic limit, these perturbations induce a phase transition from a DTC to a symmetry unbroken MBL phase[7–10], which is rounded into a crossover in finite size systems.

The phase boundary is defined by the competition between the drive perturbation ε and strength of the interactions J_0. We probe this boundary by measuring the variance of the subharmonic spectral peak height, computed over the 10 sites and averaged over 10 instances of disorder. Figure 3a shows the variances as a function of the perturbation ε, for four different interaction strengths. As we increase ε, the variance growth distinctively captures the onset of the transition, with increased fluctuations signalling the crossing of the phase boundary. When the perturbations are too large, the crystal 'melts'. The highest variances correspond to the crossover points. Figure 3b shows the fitted maxima of the variance curve, on top of numerically computed phase boundaries with experimental parameters (see Methods for the fitting
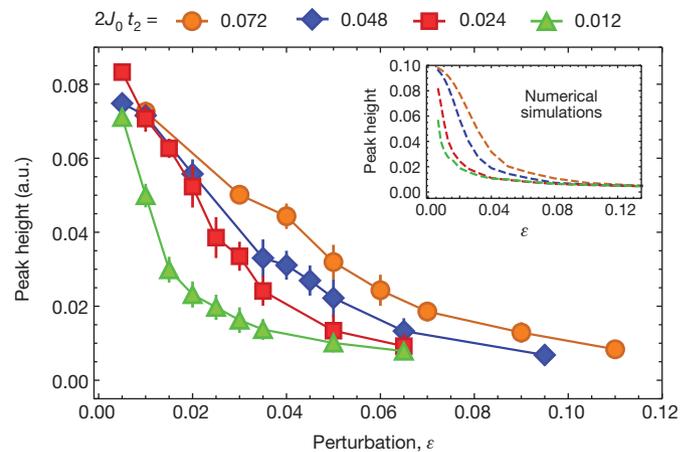
Figure 4 | Subharmonic peak height as a function of the drive perturbation. Main panel, the central subharmonic peak height in the Fourier spectrum as a function of the perturbation ε, averaged over the 10 sites and 10 disorder instances, for four different interaction strengths (see key at top). Solid lines are guides to the eye. The height decreases across the phase boundary and eventually diminishes as the single peak is split into two. Error bars, ± 1 s.d. Inset, numerical simulations given experimental parameters.

procedure). The measurements are in agreement with the expected DTC to time crystal 'melting' boundary, which displays approximately linear dependence on the perturbation strength in the limit of small interactions[10].

Figure 4 illustrates the amplitude of the subharmonic peak as a function of ε, for the four different applied interaction strengths. In the presence of spin–spin interactions, the peak height falls off slowly with increasing ε. This slope is steeper as we turn down the interaction strength, in agreement with the trend of numerical simulations (Fig. 4 inset). This is characteristic of the higher susceptibility to perturbations. This subharmonic peak height observable is expected to scale in a similar way as the mutual information[10], and can serve as an order parameter. This connection also provides insight into the Floquet many-body quantum dynamics, in particular the correlations or entanglement underlying the DTC phase. Indeed, the eigenstates of the entire Floquet unitary are expected to resemble GHZ (Greenberger–Horne–Zeilinger) or spin-'Schrödinger Cat' states[8]. The initial product state in the experiment can be written as a superposition of two cat states: $|\downarrow\downarrow\cdots\downarrow\rangle_x = \frac{1}{\sqrt{2}}\left(|\phi_+\rangle + |\phi_-\rangle\right)$, where $|\phi_\pm\rangle = \frac{1}{\sqrt{2}}\left(|\downarrow\downarrow\cdots\downarrow\rangle_x \pm |\uparrow\uparrow\cdots\uparrow\rangle_x\right)$. These two states evolve at different rates corresponding to their respective quasi-energies, giving rise to the subharmonic periodic oscillations of physical observables. Such oscillations are expected to persist at increasingly long times as the system size increases[7,8,10].

In summary, we present the experimental observation of discrete time translational symmetry breaking into a DTC. We measure persistent oscillations and synchronizations of interacting spins in a chain and show that the discrete time crystal is rigid, or robust to perturbations in the drive. Our Floquet-MBL system with long-range interactions provides an ideal testbed for out-of-equilibrium quantum dynamics and the study of novel phases of matter that exist only in a Floquet setting[7–10,25–28]. Such phases can also exhibit topological order and can be used for various quantum information tasks, such as implementing a robust quantum memory[26,29,30].

1. Chaikin, P. & Lubensky, T. *Principles of Condensed Matter Physics* Vol. 1 (Cambridge Univ. Press, 1995).
2. Wilczek, F. Quantum time crystals. *Phys. Rev. Lett.* **109,** 160401 (2012).

3. Wilczek, F. Superfluidity and space-time translation symmetry breaking. *Phys. Rev. Lett.* **111,** 250402 (2013).
4. Bruno, P. Comment on "quantum time crystals". *Phys. Rev. Lett.* **110,** 118901 (2013).
5. Bruno, P. Impossibility of spontaneously rotating time crystals: a no-go theorem. *Phys. Rev. Lett.* **111,** 070402 (2013).
6. Watanabe, H. & Oshikawa, M. Absence of quantum time crystals. *Phys. Rev. Lett.* **114,** 251603 (2015).
7. Khemani, V., Lazarides, A., Moessner, R. & Sondhi, S. L. Phase structure of driven quantum systems. *Phys. Rev. Lett.* **116,** 250401 (2016).
8. Else, D. V., Bauer, B. & Nayak, C. Floquet time crystals. *Phys. Rev. Lett.* **117,** 090402 (2016).
9. von Keyserlingk, C. W., Khemani, V. & Sondhi, S. L. Absolute stability and spatiotemporal long-range order in Floquet systems. *Phys. Rev. B* **94,** 085112 (2016).
10. Yao, N. Y., Potter, A. C., Potirniche, I.-D. & Vishwanath, A. Discrete time crystals: rigidity, criticality, and realizations. *Phys. Rev. Lett.* **118,** 030401 (2017).
11. Sachdev, S. *Quantum Phase Transitions* (Cambridge Univ. Press, 1999).
12. Li, T. *et al.* Space-time crystals of trapped ions. *Phys. Rev. Lett.* **109,** 163001 (2012).
13. Sacha, K. Modeling spontaneous breaking of time-translation symmetry. *Phys. Rev. A* **91,** 033617 (2015).
14. Nandkishore, R. & Huse, D. A. Many-body localization and thermalization in quantum statistical mechanics. *Annu. Rev. Condens. Matter Phys.* **6,** 15–38 (2015).
15. D'Alessio, L. & Rigol, M. Long-time behavior of isolated periodically driven interacting lattice systems. *Phys. Rev. X* **4,** 041048 (2014).
16. Lazarides, A., Das, A. & Moessner, R. Equilibrium states of generic quantum systems subject to periodic driving. *Phys. Rev. E* **90,** 012110 (2014).
17. Ponte, P., Chandran, A., Papic, Z. & Abanin, D. A. Periodically driven ergodic and many-body localized quantum systems. *Ann. Phys.* **353,** 196–204 (2015).
18. Else, D. V., Bauer, B. & Nayak, C. Pre-thermal time crystals and Floquet topological phases without disorder. Preprint at http://arXiv.org/abs/1607.05277 (2016).
19. Smith, J. *et al.* Many-body localization in a quantum simulator with programmable random disorder. *Nat. Phys.* **12,** 907–911 (2016).
20. Lee, A. C. *et al.* Engineering large Stark shifts for control of individual clock state qubits. *Phys. Rev. A* **94,** 042308 (2016).
21. Porras, D. & Cirac, J. I. Effective quantum spin systems with trapped ions. *Phys. Rev. Lett.* **92,** 207901 (2004).
22. Brown, K. R., Harrow, A. W. & Chuang, I. L. Arbitrarily accurate composite pulse sequences. *Phys. Rev. A* **70,** 052318 (2004).
23. Burin, A. L. Localization in a random XY model with long-range interactions: intermediate case between single-particle and many-body problems. *Phys. Rev. B* **92,** 104428 (2015).
24. Yao, N. Y. *et al.* Many-body localization in dipolar systems. *Phys. Rev. Lett.* **113,** 243002 (2014).
25. Bordia, P., Luschen, H., Schneider, U., Kanp, M. & Bloch, I. Periodically driving a many-body localized quantum system. Preprint at http://arXiv.org/abs/1607.07868 (2016).
26. von Keyserlingk, C. W. & Sondhi, S. L. Phase structure of one-dimensional interacting Floquet systems. I. Abelian symmetry-protected topological phases. *Phys. Rev. B* **93,** 245145 (2016).
27. Potter, A. C., Morimoto, T. & Vishwanath, A. Classification of interacting topological Floquet phases in one dimension. *Phys. Rev. X* **6,** 041001 (2016).
28. Jotzu, G. *et al.* Experimental realization of the topological Haldane model with ultracold fermions. *Nature* **515,** 237–240 (2014).
29. Else, D. V. & Nayak, C. Classification of topological phases in periodically driven interacting systems. *Phys. Rev. B* **93,** 201103(R) (2016).
30. von Keyserlingk, C. W. & Sondhi, S. L. Phase structure of one-dimensional interacting Floquet systems. II. Symmetry-broken phases. *Phys. Rev. B* **93,** 245146 (2016).

Author Contributions J.Z., P.W.H., A.K., P.B., A.L., J.S., G.P. and C.M. all contributed to experimental design, construction, data collection and analysis. I.-D.P., A.C.P., A.V. and N.Y.Y. all contributed to the theory for the experiment. All work was performed under the guidance of N.Y.Y. and C.M. All authors contributed to this manuscript.

METHODS

Dynamical decoupling sequence. We use a pair of Raman laser beams globally illuminating the entire ^{171}Yb$^+$ ion chain to drive qubit rotations[31,32]. The ion chain is 25 μm long, and we shape the beams to have 200 μm full-width at half-maximum along the ion chain, resulting in ∼5% intensity inhomogeneity. When a fixed duration is set for H_1 in equation (1), the time dependent magnetization for different ions acquires different evolution frequencies, resulting in the net magnetization of the system dephasing after about 10 π-pulses. In addition, the Raman laser has r.m.s. intensity noise of about 1%, which restricts the spin-rotation coherence to only about 30 π-pulses (80% contrast).

To mitigate these imperfections, we employ a BB1 dynamical decoupling pulse sequence for the drive unitary U_1 (written for each spin i):

$$U_1(\varepsilon) = e^{-iH_1 t_1} = e^{-i\frac{\pi}{2}\sigma_i^\theta} e^{-i\pi\sigma_i^{3\theta}} e^{-i\frac{\pi}{2}\sigma_i^\theta} e^{-i\frac{\pi}{2}(1-\varepsilon)\sigma_i^y}$$

where in addition to the perturbed π rotation $e^{-i\frac{\pi}{2}(1-\varepsilon)\sigma_i^y}$, three additional rotations are applied: a π pulse along an angle $\theta = \arccos\left(\frac{-\pi}{4\pi}\right)$, a 2π pulse along 3θ, and another π pulse along θ, where the axes of these additional rotations are in the x–y plane of the Bloch sphere with the specified angle referenced to the x-axis. In this way, any deviation in the original rotation from the desired value of $\pi(1-\varepsilon)$ is reduced to the third order[22].

Generating the effective Ising Hamiltonian. We generate spin–spin interactions by applying spin-dependent optical dipole forces to ions confined in a three-layer linear Paul trap with a 4.8 MHz transverse centre-of-mass motional frequency. Two off-resonant laser beams with a wavevector difference $\Delta\boldsymbol{k}$ along a principal axis of transverse motion globally address the ions and drive stimulated Raman transitions. The two beams contain a pair of beat-note frequencies symmetrically detuned from the spin transition frequency by an amount μ, comparable to the transverse motional mode frequencies. In the Lamb–Dicke regime, this results in the Ising-type Hamiltonian in equation (1)[21,33] with

$$J_{i,j} = \Omega^2 \omega_R \sum_{m=1}^{N} \frac{b_{i,m} b_{j,m}}{\mu^2 - \omega_m^2}$$

where Ω is the global Rabi frequency, $\omega_R = \hbar\Delta k^2/(2M)$ is the recoil frequency, $b_{i,m}$ is the normal-mode matrix, and ω_m are the transverse mode frequencies. The coupling profile may be approximated as a power-law decay $J_{i,j} \approx J_0/|i-j|^\alpha$, where in principle α can be tuned between 0 and 3 by varying the laser detuning μ or the trap frequencies ω_m. In this work, α is fixed at 1.5 by setting the axial trapping frequency to be 0.44 MHz, and Raman beat-node detuning to be 155 kHz.

Apply disorder in the axial direction. We apply the strong random disordered field with a fourth-order ac Stark shift[20], which is naturally an effective σ_i^z operator. To transform this into a σ_i^x operator, we apply additional π/2 rotations. Hence the third term in the Floquet evolution U_3 (written for each spin i) is also a composite sequence:

$$U_3 = e^{-iH_3 t_3} = e^{i\frac{\pi}{4}\sigma_i^y} e^{-iD_i\sigma_i^z t_3} e^{-i\frac{\pi}{4}\sigma_i^y} = e^{-iD_i\sigma_i^x t_3}$$

Experimental time sequence. The Floquet time evolution is realized using the timing sequence illustrated in Extended Data Fig. 1.

The chain of 10 trapped ions is initialized in the ground motional state of their centre of mass motion using Doppler cooling and sideband cooling (not shown). Optical pumping prepares the ions in the $|\downarrow\rangle_z$ state. We then globally rotate each spin vector onto $|\downarrow\rangle_x$ by performing a π/2 pulse around the y-axis ('Initialization' in Extended Data Fig. 1).

The H_1 Hamiltonian (perturbed π pulses) lasts 14–15 μs depending on ε and it consists of a four pulse BB1 sequence as described above. Our carrier Rabi frequency is set such that we perform a π pulse in less than 3 μs. Including the three compensating pulses, the BB1 sequence requires 5 π-pulse times to implement $U_1(\varepsilon)$.

The H_2 Ising Hamiltonian is applied for 25 μs ('Spin–spin interactions' in Extended Data Fig. 1). The pulse time was sufficiently long that with the pulse shaping described below the effects of the finite pulse time spectral broadening were largely reduced. To compensate for the residual off-resonant carrier drive, we apply a small amplitude transverse field ('Compensation' in Extended Data Fig. 1) for 2 μs.

For the H_3 disorder Hamiltonian, we apply $\sum_{i=1}^{N} D_i\sigma_i^z$ ('Strong random disorder' in Extended Data Fig. 1) generated by Stark shifts as described above. This is sandwiched between rotations around the y-axis to convert this into disorder in σ_i^x. After up to 100 applications of the Floquet evolution, we rotate the state back to the z-axis ('Prepare for measurement' in Extended Data Fig. 1) and detect the spin state $|\uparrow\rangle_z$ or $|\downarrow\rangle_z$ using spin-dependent fluorescence.

Pulse shaping for suppressing off-resonant excitations. The optical control fields for generating H_1, H_2 and H_3 are amplitude modulated using acousto-optic modulators (AOMs) to generate the evolution operators. If the rf drive to these modulators is applied as a square pulse, it will be broadened in the Fourier domain owing to fast rise and fall times at the edges (100 ns). As the pulse duration decreases, the width of the spectral broadening will expand (see Extended Data Fig. 1 inset). The components of the evolution operator must be sufficiently short in order to evolve 100 Floquet periods within a decoherence time of <8 ms.

This spectral broadening is problematic when generating the interaction Hamiltonian H_2 due to off-resonant driving. The spin–spin interactions are applied using beat-note frequencies detuned 4.8 MHz from the carrier transition and 155 kHz from the sidebands. A broad pulse in the frequency domain can drive either the qubit hyperfine transition at the carrier frequency or phonons via sideband transitions.

Similar issues occur while we apply the disordered field in H_3. The fourth-order ac Stark shift is generated from a frequency comb that has a closest beat note which is 23 MHz away from hyperfine and Zeeman transitions. To apply large average Stark shifts (33 kHz maximum) across the 10 ions, we raster the laser beam once within a single cycle (30 μs), for a single-ion pulse duration of 3 μs. The fast rastering also produces off-resonant carrier driving that resembles σ_i^y fields.

We mitigate both these effects by shaping the pulses with a 25% 'Tukey' window, a cosine tapered function for the rise and fall. This largely removes off-resonant terms in the three parts of the Floquet Hamiltonian, while minimizing the reduction in pulse area (80%). We carefully characterize any residual effects in H_2 with a single ion where no interaction dynamics are present, and apply a small compensation field in σ_i^y to cancel residual effects. We deduce an upper limit of 0.3% (relative to H_1) on the residuals from the envelopes of the dynamically decoupled π-pulse sequence.

Emergence of time crystal stabilized by the interactions and the disorder. In the main text we have shown different scenarios which occur when we modify subsections of the total Floquet evolution operator. Here we first expand the results shown in Fig. 2 of the main text by highlighting the effect of the interactions. Extended Data Fig. 2 shows individual magnetization evolutions with the same ε and instance of disorder $\{D_i\}$ but with increasing interaction J_0, from left to right. This shows how, all else being equal, as we turn up the interaction strength the synchronization across the ions gradually builds up signalling the formation of a DTC.

In a complementary fashion, Extended Data Fig. 3 addresses the role of disorder in stabilizing the time crystal formation. In particular we compare the magnetization dynamics, both in the time and the frequency domain, including or removing the disorder chapter from the total Floquet evolution. We show on the side the corresponding exact numerics calculated by applying $U(T)^N$ on the initial state $|\psi_0\rangle$ with the measured experimental parameters. Extended Data Fig. 3a shows that, with no disorder, the ion coherent dynamics tracks the perturbation ε, which results in coherent beats in agreement with our exact results. On the other hand, Extended Data Fig. 3b shows that, all else being equal, adding the disorder chapter locks the subharmonic response of all the ions. Although the numerics is qualitatively in agreement with the experimental data, nevertheless we observe a decay in the magnetization that cannot be explained by our numerical unitary simulations.

This damping can be due to two possible sources: one is the residual off-resonant drive of the disorder chapter which is not totally eliminated by the pulse shaping (see pulse-shaping section above). This small residual effect can behave like residual σ_i^x and σ_i^y terms, or coupling between the clock spin states and the Zeeman states $|F=1, m_F = \pm 1\rangle$, resulting in a decay in the coherent oscillations. This effect varies across the different disorder instances and the different interaction strengths and leads to an overall decrease of the Fourier subharmonic peak height and of its variance with respect to what is expected from the theory (see Extended Data Fig. 3b). To take this effect into account in the theory, we perform a least squares fit of the amplitude of the four theory curves to the experimental data. With this procedure we obtain scaling factors (0.56, 0.53, 0.51, 0.78) for the interaction strengths $2J_0 t_2 = (0.072, 0.48, 0.024, 0.012)$ respectively, which are consistent with the decays discussed above.

Different system sizes and initial states. We also perform the experiment with different system sizes, and show comparison with 10, 12 and 14 ions. In the thermodynamic limit, we expect the peak height order parameter to sharply decay at a certain critical perturbation strength. In our experiment this is rounded into a crossover, owing to a combination of finite size effects and long-range interactions. Extended Data Fig. 4 shows the behaviour of the subharmonic peak height as we gradually add more ions to the spin system. The slope clearly sharpens up to 14 ions. We show a phenomenological scaling in the inset of Extended Data Fig. 4, when collapsing the three curves on top of each other.

Another interesting check is the time crystal dynamics under different initial conditions. In the data presented in the main text, we started from all spins

polarized in the same direction. However, the time crystal dynamics in the MBL regime should exhibit little dependence on the initial state, and should in fact manifest the rigidity with arbitrary initial conditions. We observe that this is indeed the case, for example in a different initial state that has the left half of the spins anti-aligned with the right half. Indeed we see that the ions are synchronized by the interactions, and oscillate either in-phase or out-of-phase, retaining memory of the initial states (left panel of Extended Data Fig. 5). The right panel of Extended Data Fig. 5 shows the peak height observable, and the inset shows the fast Fourier transform (FFT) subharmonic response.

Data analysis and fitting procedure. The peak height variance data in Fig. 3a are fitted to a lineshape in order to extract the crossover transition boundary ε_p in Fig. 3b. We use the following phenomenologial lineshape, a Lorentzian of the $\log_{10}(\varepsilon/\varepsilon_p)$:

$$F(\varepsilon) = A \frac{1}{1 + \left(\frac{\log_{10}(\varepsilon/\varepsilon_p)}{\gamma} \right)^2} + B \tag{3}$$

A statistical error is extracted from a weighted nonlinear fit to the data, which yields a fractional standard error bar of a few per cent. The error in the peak height is limited by systematic error in the finite number of instances we realized in the experiment. For each value of J_0 and ε we average over the same 10 instances of disorder. These 10 instances are averaged and fitted to $F(\varepsilon)$.

In order to estimate the error due to the finite disorder instances, we perform random sampling from a numerical dataset of 100 instances of disorder. Sampling 10 of these and fitting the peak height variance data to $F(\varepsilon)$ yields a Gaussian distribution of extracted peak centres ε_p over 10,000 repetitions (Extended Data Fig. 6). We take the one standard deviation (67%) confidence interval in the sample as the systematic uncertainty in the fit, which yields a fractional error of ~15%. This systematic uncertainty dominates over the statistical, so we apply error bars in Extended Data Fig. 3b equal to this computed finite sampling error.

Data availability. The data that support the plots within this paper and other findings of this study are available from the corresponding author upon reasonable request.

31. Olmschenk, S. *et al.* Manipulation and detection of a trapped Yb$^+$ hyperfine qubit. *Phys. Rev. A* **76,** 052314 (2007).
32. Hayes, D. *et al.* Entanglement of atomic qubits using an optical frequency comb. *Phys. Rev. Lett.* **104,** 140501 (2010).
33. Kim, K. *et al.* Entanglement and tunable spin-spin couplings between trapped ions using multiple transverse modes. *Phys. Rev. Lett.* **103,** 120502 (2009).
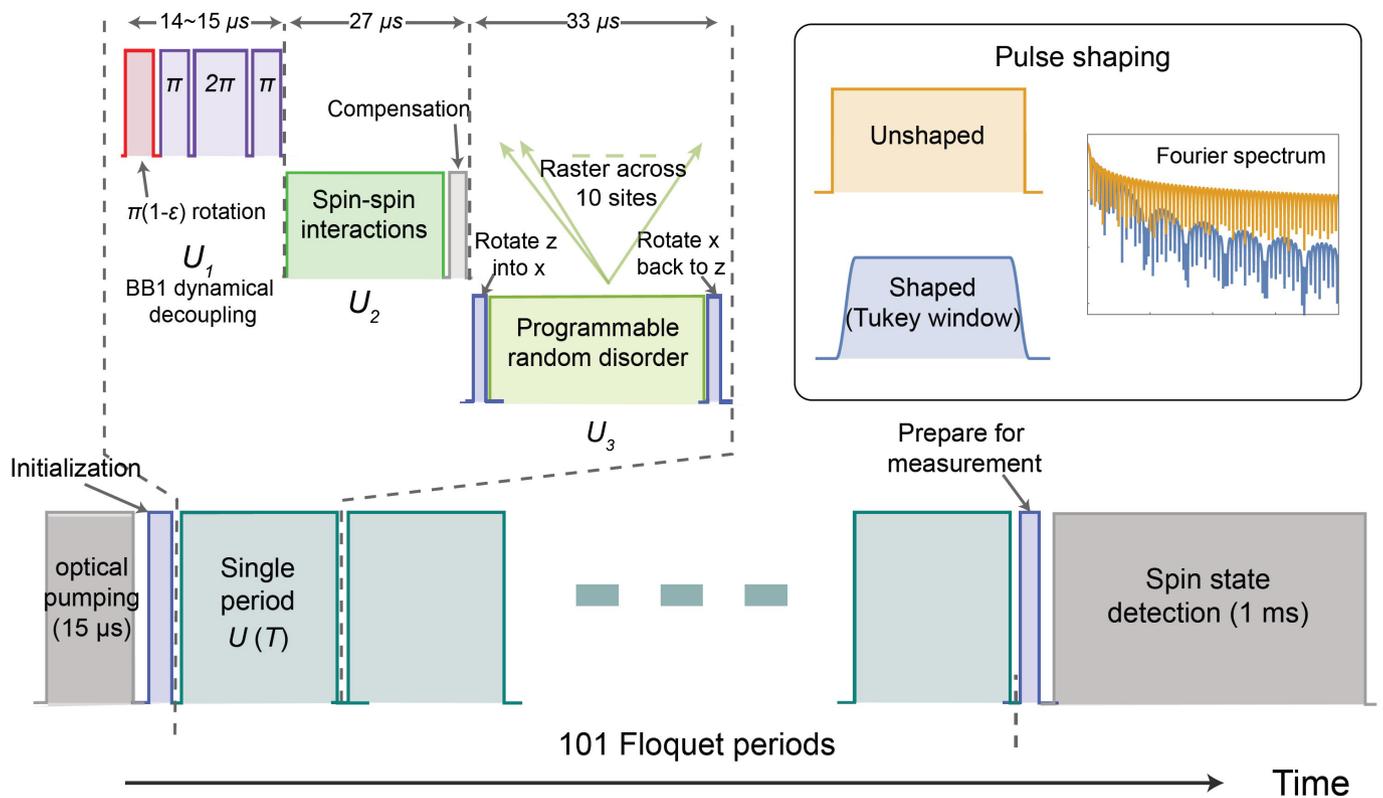
Extended Data Figure 1 | Experimental pulse sequence. Bottom left, we initialize the spins via optical pumping plus a spin rotation, and then start the Floquet evolution. Each period includes the three parts of the Hamiltonian as described in the main text and Methods (top left), and is repeated for 100 times. We then perform an analysis rotation to the desired direction on the Bloch sphere, and then perform spin state detection (bottom right). Inset at top right, all pulses in the Floquet evolution are shaped with a 'Tukey' window. See text for detailed explanations.
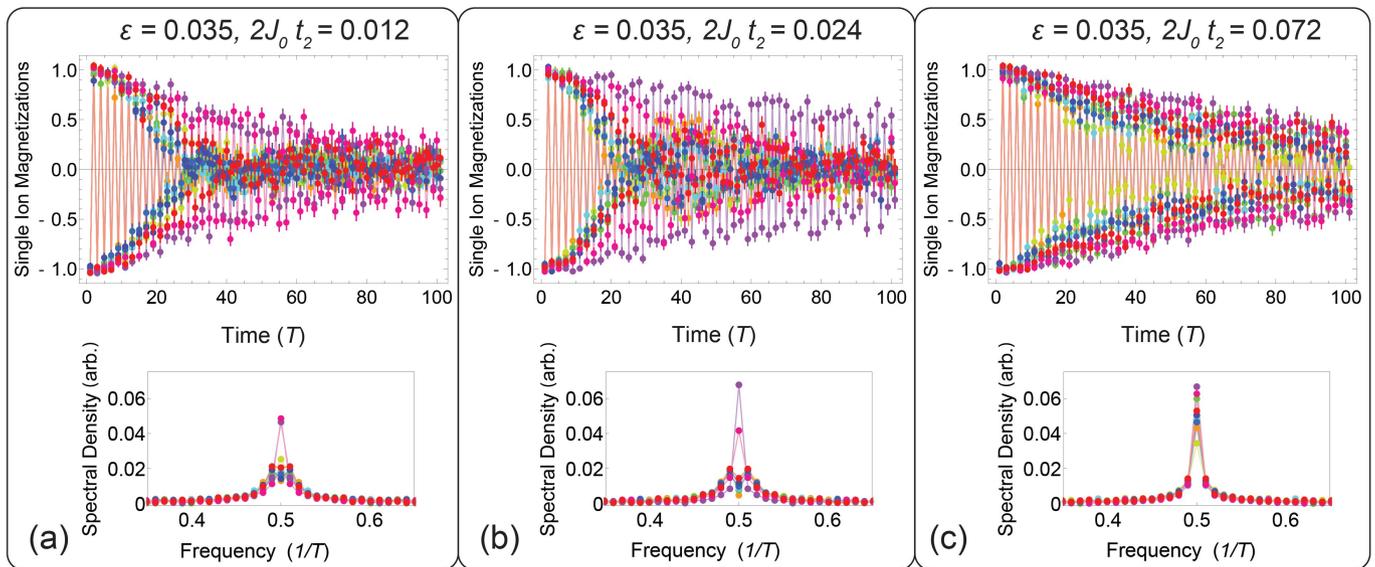
Extended Data Figure 2 | Build-up of a DTC. From **a** to **b** to **c**, we fix the disorder instance (that is, a single sample of the random disorder realizations) and the perturbation ε, while gradually increasing the interactions ($2J_0 t_2$) for different experimental runs. The temporal oscillations are synchronized with increasing interactions, and the Fourier subharmonic peak is enhanced. The top panel shows the time-traces of the individual spin magnetizations, and the bottom panel shows the Fourier spectrum.
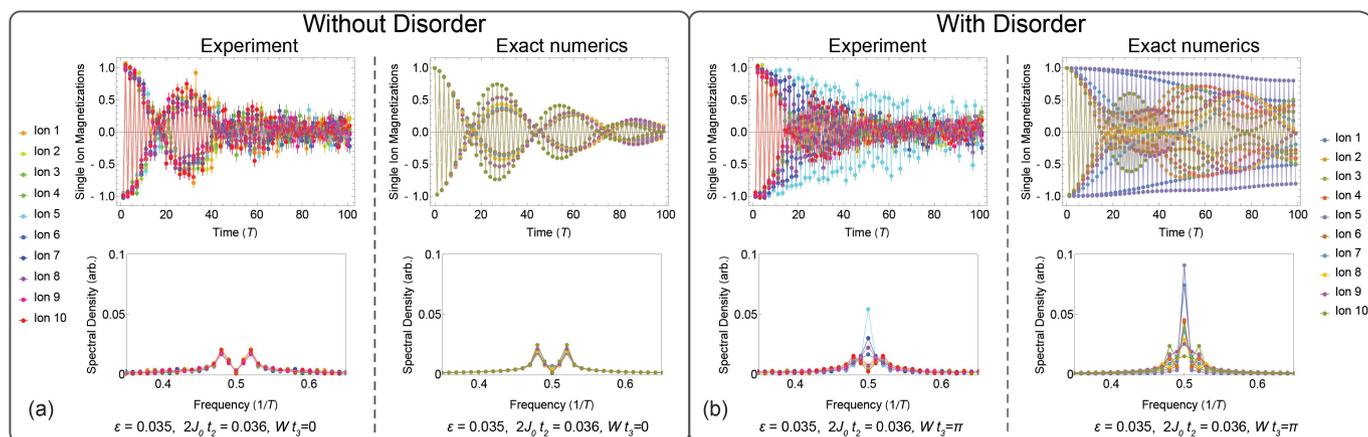
Extended Data Figure 3 | Comparing the ions' dynamics with and without disorder. a, Without disorder ($W_0 t_3$ set to 0), the spin–spin interactions suppress the beatnote imposed by the external perturbation ε. Left, experimental data; right, exact numerics calculated under Floquet time-evolution. **b**, With disorder ($W_0 t_3 = \pi$), the time crystal is more stable. Left, experimental result for a single disorder instance; right, numerical simulations. The top panels show the individual spin magnetizations as a function of time, and the bottom panels shows the Fourier transforms to the frequency domain.
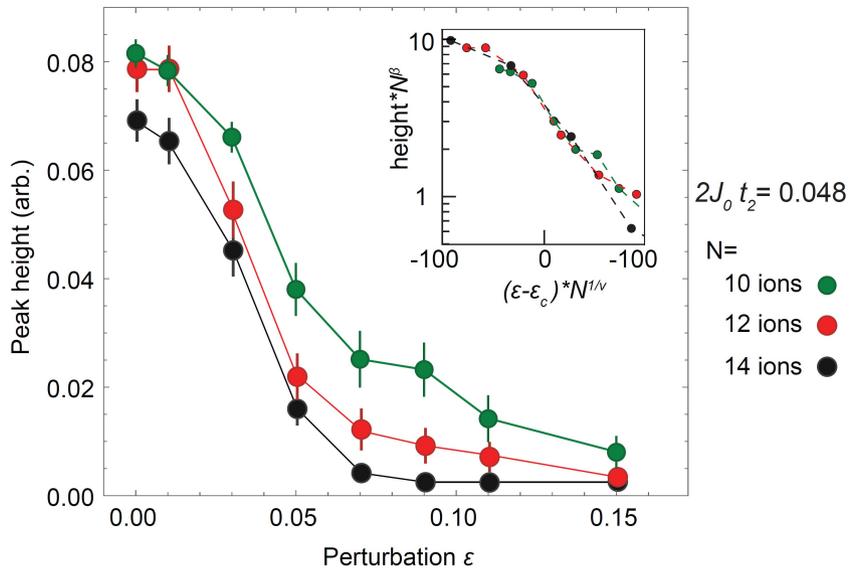
Extended Data Figure 4 | Finite size scaling. Shown are subharmonic central peak heights as a function of the perturbation, for different numbers of ions, $N = 10$, 12, and 14. We observe a sharpening, that is, that the curvature of the slope is increasing, as the chain size grows, consistent with expectations. Each curve contains one disorder realization, which is a single sample of random instance with $W_0 t_3 = \pi$, but the data are averaged over all the ions (yielding the error bars shown). Inset, phenomenological scaling collapse of the three curves[10], with the following parameters: $\varepsilon_c = 0.041$, $v = 0.33$, $\beta = 1.9$, which are critical exponents following the analysis in ref. 10. The extracted value of ε_c is consistent with the interaction strength, which is fixed at $2J_0 t_2 = 0.048$ throughout this dataset.
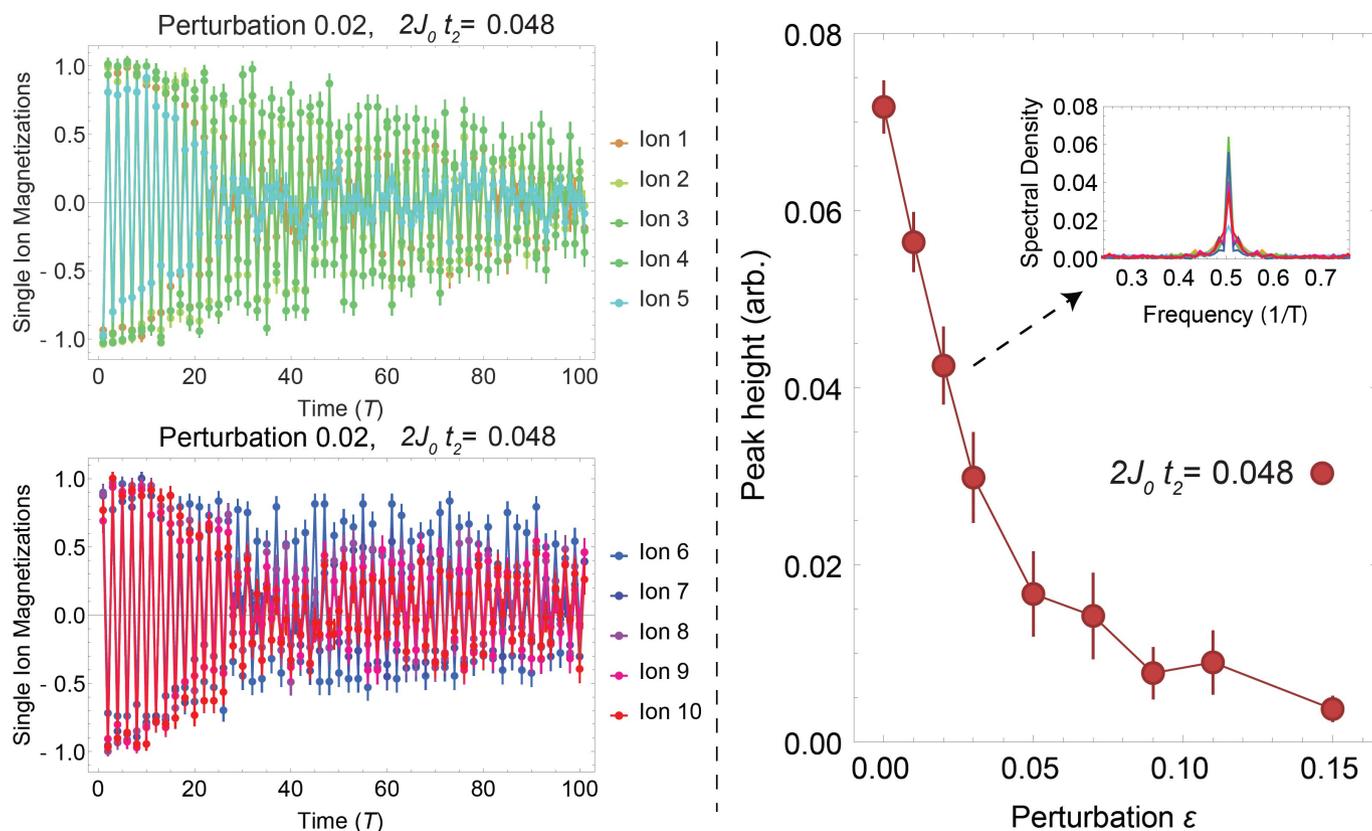
Extended Data Figure 5 | Different initial states. Starting with the left half of the chain initialized in the opposite direction, we observe that the time crystal is still persistent in the presence of perturbations. Top left, time-dependent magnetizations for ions in the first half of the chain. Bottom left, magnetizations for the second half. Notice that the spins on the two halves oscillate with opposite phases throughout, until the end of the evolution. Right, average peak height as a function of perturbation. Inset, FFT spectrum for 2% perturbation. $2J_0 t_2$ was fixed at 0.048 throughout this dataset.
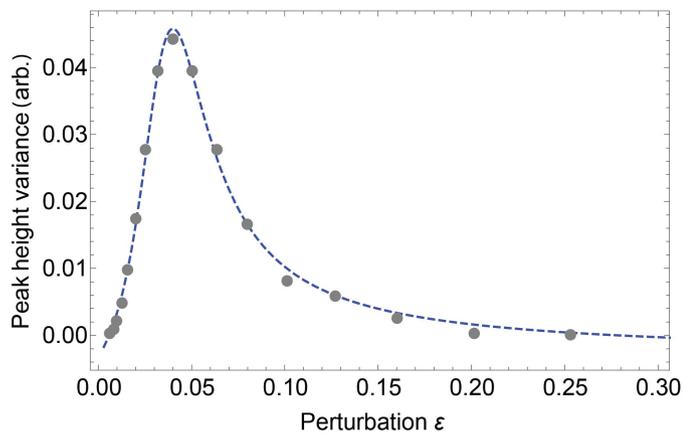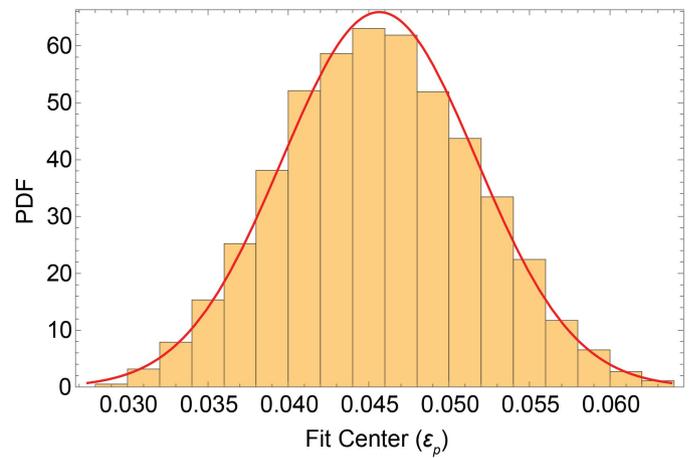
Extended Data Figure 6 | A random sampling from numerical evolutions. Shown are averages of 10 disorder instances from numerical evolution under H for $2J_0 t_2 = 0.072$. Left, an example random numerical dataset (points) and the fit to equation (3) in Methods (dashed line). Right, the normalized probability distribution (PDF) of peak fit centres ε_p is shown in yellow, and a normal distribution is overlaid in red. The normal distribution is fitted using only the mean and standard deviation of the sample, showing excellent agreement with Gaussian statistics. For this value of J_0 the mean $\bar{\varepsilon}_p = 0.046$ and the standard deviation $\sigma\varepsilon_p = 0.006$.